Journal Name

ARTICLE TYPE

Cite this: DOI: 10.1039/xxxxxxxxxx

Magnetically driven omnidirectional artificial micro-swimmers†

Mojca Vilfan,*[a] Natan Osterman,[a,b] and Andrej Vilfan[a]

Received Date
Accepted Date

DOI: 10.1039/xxxxxxxxxx

www.rsc.org/journalname

We present an experimental realisation of two new artificial microswimmers that swim at low Reynolds number. The swimmers are externally driven with a periodically modulated magnetic field that induces an alternating attractive/repulsive interaction between the swimmer parts. The field sequence also modulates the drag on the swimmer components, making the working cycle non-reciprocal. The resulting net translational displacement leads to velocities of up to 2 micrometers per second. The swimmers can be made omnidirectional, meaning that the same magnetic field sequence can drive swimmers in any direction in the sample plane. Although the direction of their swimming is determined by the momentary orientation of the swimmer, their motion can be guided by solid boundaries. We demonstrate their omnidirectionality by letting them travel through a circular microfluidic channel. We use simple scaling arguments as well as more detailed numerical simulations to explain the measured velocity as a function of the actuation frequency.

Introduction

Transport of biological and artificial nano- to micro-scale objects presents a fascinating problem that has gained a lot of attention in the recent years. Its main feature lies in the low Reynolds number (LRN), a hydrodynamic regime in which the inertia is negligible, the motion is dominated by the viscous forces, and since the fluid flows are time reversible, swimming under such conditions requires non-reciprocal motion[1]. Many manifestations can be found in nature, as the motion of micron-sized organisms falls under the LRN regime. Rotating flagella of bacteria, travelling waves on spermatozoa flagellum, and beating cilia of many motile eukaryotic organisms are just a few examples[2].

Several theoretical studies proposed simple concepts how to produce non-reciprocal motion and directed swimming with arrangements of a small number of particles. The swimmer by Najafi and Golestanian[3] is composed of three linked spheres and swims by periodically yet non-reciprocally changing the lengths of the links. This model has later been extended to a circular swimmer[4] and to larger particle assemblies[5,6]. Another simple model, the so-called *pushmepullyou* by Avron and co-workers[7], is made up of two spherical bladders that periodically change their separation and volumes to produce locomotion. If an external torque (e.g. magnetic) is applied to the swimmer, non-reciprocal motion can even be achieved with two particles of constant volume[8–10]. While the hydrodynamic interactions[11] that give rise to swimming are well understood, the experimental realization of such swimmers is not straightforward.

Most experimentally realized many-body swimmers used an externally applied periodic magnetic field sequence to modulate the interactions between particles and to induce torques on the assemblies. The field can be either oscillating, rotating, or, simply, contain a gradient[12]. Dreyfus et al.[13] were the first to create artificial flagella by assembling an elongated structure and driving it with an oscillating magnetic field. Elastic deformations make the motion non-reciprocal and enable directed propulsion[14]. A similar effect can be achieved with a buckling filament[15]. Tierno et al.[16] designed a magnetically-actuated swimmer whose propulsion was assisted by a boundary rather than by body deformations. Two more swimming mechanisms based on the interactions with the boundary were demonstrated by Morimoto et al., who observed tumbling motion on a magnetic substrate[17], and by Sing et al., who created artificial walkers as long chains of superparamagnetic particles[18]. Colloidal wheels rolling along a surface were shown to exhibit very interesting non-reciprocal dynamics[19]. Further experiments include propulsion of rotating microscopic helices[20–23] and spiral motion of a particle-based microswimmer[24]. Helical microswimmers, in particular, were studied as candidates for microrobots in biomedical applications such as targeted drug delivery, micro-surgery, sensing or detoxification[12,25,26]. A common limitation of all these designs is that the direction of swimming is uniquely determined by the magnetic field sequence. It is therefore not possible to have different swimmers simultaneously moving in different directions.

[a] J. Stefan Institute, Jamova 39, 1000 Ljubljana, Slovenia; E-mail: mojca.vilfan@ijs.si
[b] Faculty of Mathematics and Physics, University of Ljubljana, Jadranska 19, 1000 Ljubljana, Slovenia.

† Electronic Supplementary Information (ESI) available. See DOI: 10.1039/b000000x/

Alternative propulsion mechanisms for swimmers, such as chemical catalysis[27,28], electric field (Quincke effect)[29], light[30] and ultrasound[31] do not come with this limitation. In these cases the swimming direction is determined by the orientation of the particles or by small initial perturbations. Magnetic rollers can also be driven with an oscillating vertical field alone, but only if they are large enough that inertial effects play a role[32]. Such swimmers were therefore widely used to study collective phenomena, such as flocking[29,32].

In this paper, we present an experimental realisation of two magnetically driven omnidirectional swimmers in water. The first swimmer type, we name it *the thrower*, is composed of a large and a small sphere, with the smaller one being repeatedly "thrown" away from the large one. The second type, called *the rower*, comprises a small sphere and a dumbbell made of two spheres. The orientation of the dumbbell during the cycle loosely follows the orientation of an oar, hence the name. Both swimmer types are actuated externally with a magnetic field that periodically alternates between an attractive and a repulsive interaction. The thrower breaks the time reversal symmetry because the small sphere follows different trajectories during the repulsive and attractive phases. The rower achieves a similar effect by different orientations of the dumbbell. The described swimmers are omnidirectional – meaning that the direction of their movement in the plane is determined by the orientation of the swimmer and not by the direction of the external magnetic field as in most magnetically-actuated swimmers. Guided by microchannels, they can autonomously travel through complex microfluidic networks. They can travel individually or collectively, making them suitable for studying collective dynamics where all the swimmers are driven by the same external force, yet move through complex formations of channels with no pre-programmed magnetic sequence.

Swimming mechanisms

To achieve alternating attractive and repulsive magnetic forces between the swimmer components, superparamagnetic beads were used in the experiment. Here the term superparamagnetic is used in the sense that without the magnetic field, the magnetisation in the spheres – and with it magnetic interaction between the spheres – is zero. When magnetic field is switched on, magnetisation, which is proportional to the external magnetic field and parallel to its direction, is induced. The beads then interact via magnetic dipole-dipole interaction. Depending on the orientation of the dipoles, the force between the beads can be either attractive or repulsive.

Repulsive force between the swimmer components was obtained when the external magnetic field was oriented in the vertical direction (perpendicular to the observed motion), whereas the attractive force was achieved with the magnetic field in the sample plane. This attractive force, however, only acts in the direction of the external magnetic field. To obtain a uniform and isotropic attractive interaction between the beads, magnetic field can be rotated in the sample plane, so that the inter-particle force rapidly changes from attractive to repulsive and back. Since the two forces differ in amplitude, the average in-plane dipole-dipole force is attractive. This method thus enables generation of both isotropic repulsive and isotropic attractive force between particles in the sample plane.

We first describe the swimming mechanism of the thrower, which comprises two beads of different size, both heavier than water. The swimming cycle starts with the beads in contact (Figure 1a). When a strong repulsive force between the beads is applied (Figure 1b), the beads are pushed apart whereby the smaller bead largely follows a horizontal path. Afterwards, the force is turned off and the small bead is left to sediment (Figure 1c). After the pause, attractive force is applied (Figure 1d) and the beads are drawn together. However, the smaller bead now follows a different path, closer to the bottom plate (Figure 1e). Finally, the smaller bead returns to the initial position, but the whole swimmer has moved (Figure 1f).

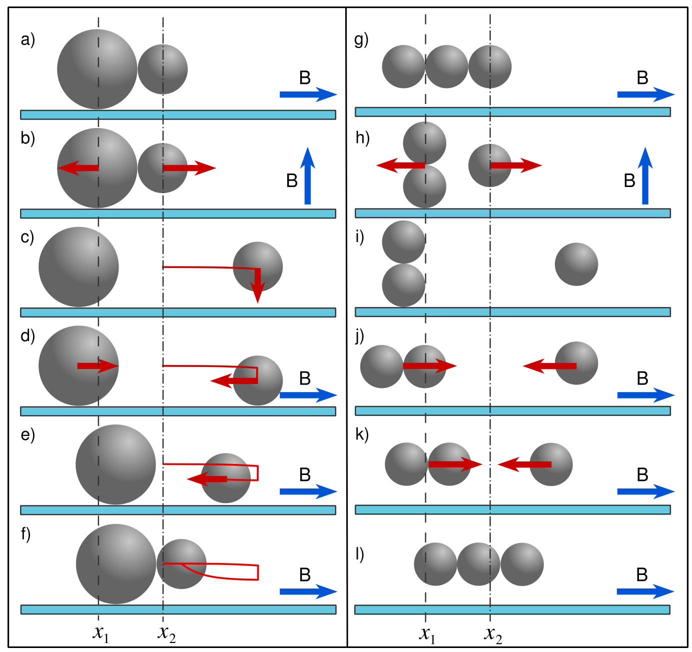

Fig. 1 Simplified motion mechanism for the thrower (left) and rower (right). Blue arrows denote the direction of the external magnetic field, red arrows indicate the directions in which the swimmer components are moving, and the continuous red line on the left presents the path of the smaller sphere during one cycle.

The propulsion mechanism can be understood as follows. Let x_1 denote the horizontal position of the large bead (radius a_1) and $x_2 > x_1$ that of the small one (radius a_2). We write down the equations of motion for the horizontal positions of both beads,

$$\dot{x}_1 = -F\mu_{11} + F\mu_{12} \tag{1}$$

$$\dot{x}_2 = -F\mu_{21} + F\mu_{22} \tag{2}$$

where the force F has a positive sign when it is repulsive and negative when it is attractive. The parameters μ_{11} and μ_{22} are the mobilities of the large and the small particle, respectively, and $\mu_{12} = \mu_{21}$ is the term describing hydrodynamic interactions between them. It should be noted that the mobility of the smaller particle μ_{22} depends on its elevation z_2 and that the interaction term μ_{12} depends on both the elevation and the separation between the beads. Both μ_{22} and μ_{12} therefore vary during the cycle. We neglected the off-diagonal mobility terms that describe the horizontal motion of a particle due to the vertical force acting on the other one or vice versa. We now introduce the parameter $Y = x_2 - x_1$, which describes the distance between the centres of the spheres. From Eqs. 1 and 2 it follows

$$\dot{Y} = F(\mu_{22} + \mu_{11} - 2\mu_{12})\,. \tag{3}$$

Through a cycle, the distance changes from its minimum value $Y_0 = a_1 + a_2$ to a maximum Y_1 and back. The total shift of the position of the large sphere in one cycle can therefore be written as

$$\Delta x_1 = -\oint \frac{\mu_{11} - \mu_{12}(z_2,Y)}{\mu_{22}(z_2) + \mu_{11} - 2\mu_{12}(z_2,Y)} dY. \tag{4}$$

During the repulsive part of the cycle, when $dY > 0$, the smaller sphere is further away from the surface and z_2 is larger than during the attractive phase (when $dY < 0$). Consequently, $\mu_{22}(z_2)$ is larger during this part of the cycle. Taking into account that the coupling mobility μ_{12} is much smaller than the diagonal mobilities, it follows that the net displacement in a complete cycle is positive and $\Delta x_1 > 0$.

The frequency dependence of the swimming velocity follows from the following considerations. For two spheres whose centres are at the same height (which is roughly the case in the repulsive phase), the magnetic dipole-dipole interaction force scales with $\sim Y^{-4}$. Neglecting hydrodynamic interactions in Eq. 3, this leads to a solution $Y^5 - Y_0^5 \sim t$. The maximum separation during the cycle is reached at the end of the repulsive phase, whose duration is inversely proportional to the frequency f, and therefore has a frequency dependence of $Y_1 \sim f^{-1/5}$. At lower frequencies, the small particle approximately keeps the initial vertical position during the short repulsive phase, but sediments to the bottom during the phase without a field. During the attractive phase, it remains close to the bottom the longest part of the approach. We can therefore use $z_2 \approx a_1$ for the repulsive and $z_2 \approx a_2$ during the attractive phase. The integral in Eq. 4 is then proportional to ΔY. Finally, we can calculate the swimming speed v, which is the displacement per cycle, multiplied by the frequency f

$$v = \Delta x_1 f \tag{5}$$

and scales as $v \sim f^{4/5}$.

At higher frequencies the phase without the magnetic field is too short for the small particle to sink to the bottom. The vertical displacement during the field-free phase is then proportional to its duration $\delta z_2 \sim f^{-1}$. For small differences in height, the integral in Eq. 4 is proportional to the area enclosed by the small particle's trajectory. Its width scales as $\Delta Y \sim f^{-1/5}$ and its height as $\sim f^{-1}$. The integral in Eq. 4 then scales as $\sim f^{-6/5}$ and the velocity with $\sim f^{-1/5}$.

The cross-over frequency between the two regimes can be estimated from the sedimentation time of the small particle from a starting point determined by the radius of the larger one, $z_2 = a_1$. The vertical drag coefficient at this height is about 3× the unbounded Stokes drag, giving a sedimentation velocity of $1\,\mu$m/s. This gives a sedimentation time of approx. 1 s (an exact calculation gives 1.4 s). With 38 % of the cycle in the off state, we finally obtain a cross-over frequency of ~ 0.4 Hz.

The swimming mechanism of the second swimmer, the rower, works as follows. The rower is composed of three beads with radius a_2, two of which form a dumbbell. The cycle starts with the dumbbell aligned horizontally at $x_1 = 0$ and the single sphere at $x_2 = 3a_2$ (Figure 1g). When an external magnetic field pointing in the vertical direction is applied (Figure 1h), the dumbbell quickly reorients and the repulsive force pushes the single bead away from the dumbbell. Since the drag on the dumbbell is larger than on a single sphere, the single sphere moves further than the couple (Figure 1i). The magnetic field is then switched to horizontal direction, the dumbbell quickly rotates (Figure 1j) and the attractive force draws the spheres together (Figure 1k). However, the drag on the rotated dumbbell is now reduced and the swimmer's centre of mass moves to the right (Figure 1l).

Experimental

The throwers were created by using pairs of superparamagnetic beads with diameters $2a_1 = 4.5\,\mu$m and $2a_2 = 2.7\,\mu$m (Dynabeads Epoxy M-450 and M-270, both Dynal Biotech[33]). The microspheres were mixed in ultra-pure water (Millipore, 18.2 MΩcm) with added surfactant SDS (sodium dodecyl sulphate, 5 mg/ml) to prevent sticking and aggregation of the beads. A droplet of the mixture was placed on a microscope slide and covered with a cover slide, pressed and sealed to prevent evaporation and fluid currents in the cell. As the distance from the surface plays an important role in this experiment, wedge cells were prepared, enabling us to choose the appropriate sample thickness, varying from a few microns to several tens of microns.

The rowers comprised three spheres with a diameter of $2a_2 = 2.7\,\mu$m, two of which were non-specifically bound forming a dumbbell. The samples were prepared similarly as for throwers with two different sample thicknesses d: one larger than the dumbbell size $d > 4a_2$, and one slightly smaller than twice the bead diameter $d < 4a_2$.

To facilitate the velocity measurements, we first applied an attractive potential that kept the swimmers aligned with the x-axis, thus making them bi-directional instead of omnidirectional. The magnetic field density used in the experiments was 10.5 mT for repulsive and 1.77 mT for attractive force. One complete swimming cycle was achieved by using the following magnetic field sequences. For the thrower 1 % in $+z$ direction, 19 % no magnetic field, 30 % in the plane ($+x$) direction, followed by 1 % in $-z$ direction, 19 % no magnetic field, and 30 % magnetic field in $+x$ direction. Magnetic field sequence for the rower was 45 % attractive ($+x$), 5 % repulsive ($+z$), 45 % attractive ($+x$), and 5 % repulsive ($-z$). The asymmetric cycle was employed to make the field sequence spatially symmetric and prevent biased rotation and rolling of the beads. For omnidirectional swimmers, the horizontal field was rotated around the z axis with a frequency of 400 Hz in alternating directions. To exclude any possible effects of field gradients and flow of the surrounding fluid, we acquired the velocities of several swimmers moving simultaneously in opposite directions. The experiments were also made with swimmers moving in the $+y$ and $-y$ directions, but no significant difference was observed.

We used the experimental set-up described previously[34,35]: an optical microscope (Zeiss Axiovert 200M inverted microscope, Achroplan 63/0.9*W* objective) additionally equipped with three orthogonal pairs of coils. Electrical currents through the coils were regulated individually creating an almost homogeneous magnetic field of varying magnitude in arbitrary direction. The motion of the particles was recorded in the bright field with a CMOS camera (Pixelink, PL-A741) and analysed with a particle tracking software (PartTrack, Aresis).

Results and discussion

Throwers

A representative example of observed thrower traces is shown in Figure 2, together with the traces of single beads undergoing Brownian motion. For clarity, initial positions of all the swimmers and beads were set to zero. We oriented the swimmers such that two of them were swimming in the $+x$ direction and two in the $-x$ direction, and the contrast between their directed motility and the Brownian motion of isolated single particles is clearly visible. The average diffusion constant of the non-swimming beads with the radius of $a_2 = 1.4\,\mu$m was found to be $D_1 = (7.2 \pm 1.0) \times 10^{-14}\mathrm{m}^2/\mathrm{s}$, which is notably lower than the expected diffusion coefficient of the same particles in bulk water $D_0 = k_B T/(6\pi a_2 \eta) = 16 \times 10^{-14}\mathrm{m}^2/\mathrm{s}$. The difference can be explained with the particle's proximity to the no-slip boundary on the surface. Considering Boltzmann's distribution of particles in the gravitational field, one would expect an average distance of 90nm. The observed reduction in diffusion constant (equivalent to a reduction in mobility) is obtained if the distance between the particle and the surface is $0.1\,a_2 = 140\,\mathrm{nm}$[36].

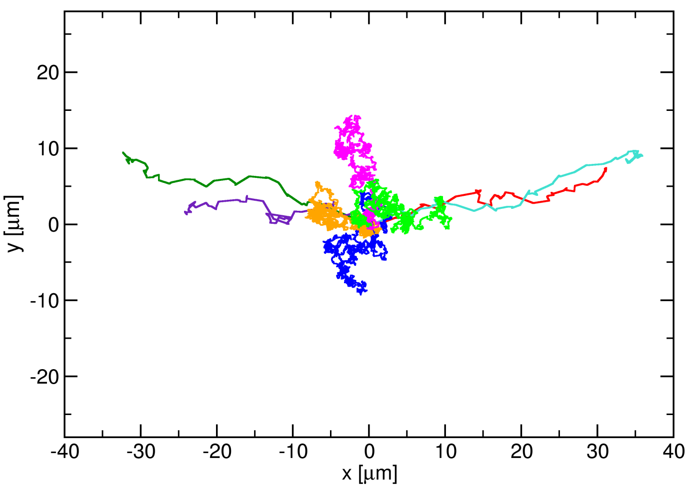

Fig. 2 Traces of four throwers (green, violet, red and cyan) and traces of four individual beads (orange, bright green, blue and magenta) taken from the same measurement at a modulation frequency of $f = 4$ Hz.

Taking a closer look at the traces, we can separately plot positions of the larger and the smaller bead. In Figures 3a and 3b observed bead positions $x_1 + a_1$ (black) and $x_2 - a_2$ (red) are shown for an attraction-repulsion cycle frequency of 0.3 Hz and 8 Hz, respectively. Their motion averaged to one cycle is presented in Figures 3c and 3d. One clearly observes the different stages of the cycle: the rapid repulsion, when the beads are pushed apart, the off-time, when the smaller bead sediments, and the gradual decrease in the separation when attractive force acts between the beads. Due to a lower amount of data in the slow motion, the averaged curve is not as smooth, but the increase in the maximal separation value Y_1 is still apparent. The same motion was also numerically simulated and the obtained averaged curves, which are shown in Figures 3e and 3f, are in a very good agreement with the observed ones. The additional information that one can acquire from the numerical simulations are the elevations of the individual beads, which are the crucial parameter in the efficiency of motion. The elevations are shown in Figures 3g and 3h for lower and higher frequency, respectively. The black lines show the elevation of the larger bead, which clearly does not change during the cycle. The motion of the smaller bead (red line) will be discussed later.

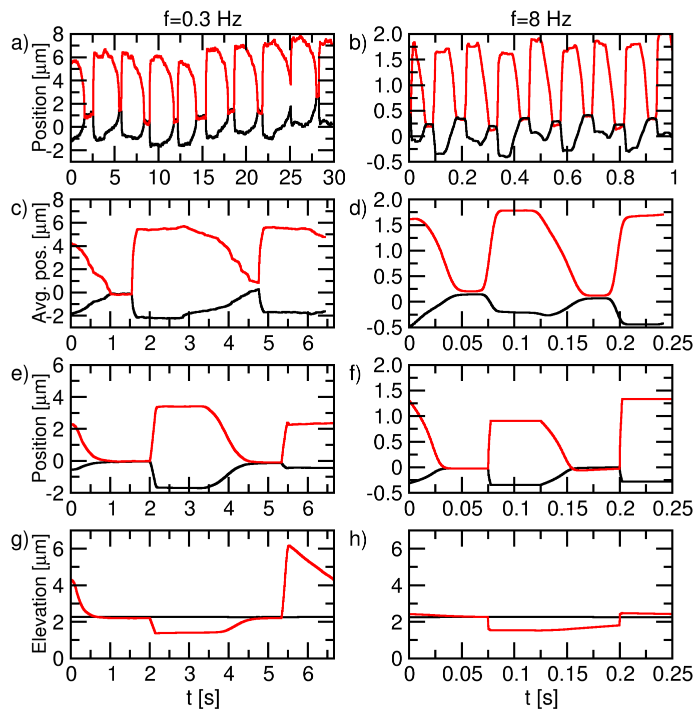

Fig. 3 Positions of the beads at low frequency (left column) and at high frequency (right column): (a) and (b) measured positions of the beads $x_1 + a_1$ (black) and $x_2 - a_2$ (red) as a function of time with corresponding averaged traces shown in (c) and (d). Averaged bead positions (e) and (f) and their elevations (g) and (h) from numerical simulations. Red lines always denote the position or elevation of the smaller bead and black of the larger one.

The traces of motion can be used to obtain the swimming velocities as a function of attraction-repulsion cycle frequency f, which are shown in Figure 4 as red dots. The frequency dependence of velocity - initial increase and subsequent decrease - is in qualitative agreement with the predictions of the simple model (Eqs. 1-5). A more exact numerical simulation of the system, without free parameters, is described in the Appendix and shown by the dashed line in Figure 4. Interestingly, there is a big discrepancy at frequencies below $\sim 2\,\mathrm{Hz}$. Most visibly, the experimentally ob-

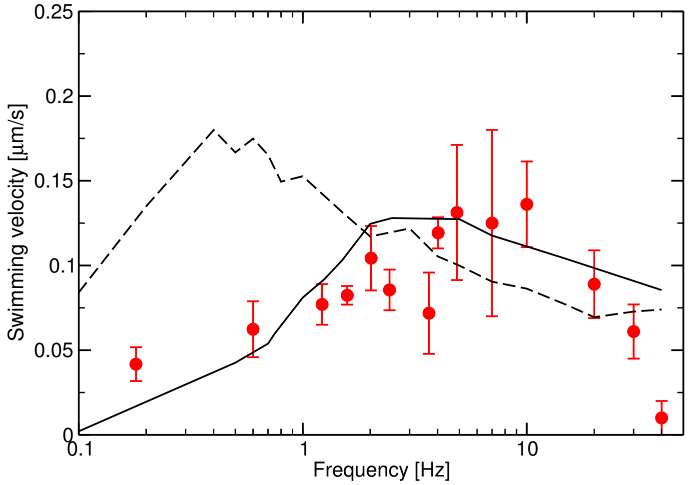

Fig. 4 Swimming velocity of the thrower as a function of the cycle frequency. Red circles: experimentally measured velocities. Dashed line: simulation of the basic model. Solid line: simulation taking into account bead rotation during the switch from attractive to repulsive interaction.

served maximal velocity is reached at frequencies around 5 Hz, rather than 0.4 Hz as predicted.

As seen in some of the recorded videos†, the small bead follows different trajectories during even and odd cycles, which differ by the direction of the vertical magnetic field. This observation can be explained by the anisotropy and finite magnetic relaxation rate, which had been reported in Dynabeads before[37]. When the field alternately switches from horizontal to vertical up or down, this causes a quick rotation of the large bead. Because of hydrodynamic interactions or adhesion between the beads, the small bead follows the rotation for a short time, meaning that it is slightly shifted upwards or downwards at the onset of the repulsive phase, as shown in Figure 5. As a consequence, the area enclosed by the trajectory of the small bead is reduced at low frequencies, which lowers the swimming velocity. At the same time, the rotation introduces a non-reciprocity into the trajectory that is independent of gravity. The swimming velocities are therefore increased at high frequencies. The angle of rotation can be estimated if we assume that the small bead remains close to the surface of the large one while the latter turns by an angle of $\pi/2$. Because the angular velocity of the fluid around a rotating sphere shows a $\sim r^{-3}$ dependence[38], we expect a rotation of the small bead around the large one by an angle $\alpha \approx (a_1/(a_1+a_2))^3\pi/2 = 0.38\,\mathrm{rad}$. In reality the distance between the beads starts growing before the turn is completed. We thus treat the effect phenomenologically by using a somewhat smaller angle $\alpha_\pm = \pm 0.16\,\mathrm{rad} \approx \pm 9°$, which leads to a good agreement with the measurements. The simulated swimming velocity is shown by the solid line in Fig. 4.

The additional asymmetry that is introduced with the slight rotation is best visible in the elevation plot, shown in Figures 3g and 3h. The constant black line is the elevation of the larger sphere, which does not change during the cycle, and the red line denotes the elevation of the smaller sphere. At higher frequencies (Figure 3h), the effect of the rotation on the swimming velocity is rather small as the sphere always remains at a notable elevation above the surface. This is different in the case of low frequencies (Figure 3g), where the motion becomes highly asymmetric, since the vicinity of the surface and anisotropic magnetic interaction effectively reduce the step length and with it the average swimming velocity.

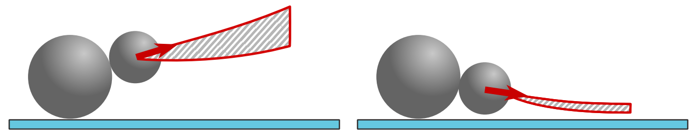

Fig. 5 Schematic representation of the additional asymmetry introduced into the system by slight rotation of the large bead

So far, the throwers were swimming in either $+x$ or $-x$ direction simultaneously. If instead of horizontal magnetic field a rotating in-plane magnetic field is applied, the swimmers start swimming in arbitrary directions in a non-predetermined manner. However, the swimming velocity is reduced to below 100 nm/s.

Omnidirectional Rower

The second swimmer, the rower, does not require the proximity of the surface to move. The broken time reversal symmetry is achieved by rotating the dumbbell and thus changing the drag on one swimmer component during the cycle (Figures 1 g-l). The swimming efficiency and velocity, however, are significantly increased if the swimmer is placed between two flat surfaces. In thin samples, in which the separation between the surfaces is slightly smaller than the size of the dumbbell ($d < 4a_2$), the dumbbell wedges between the glass plates, which strongly increases its drag during the repulsive phase.

The observed swimming velocity of the bidirectional wedged rower as a function of the cycle frequency is shown in Figure 6. In contrast to the thrower, the velocity reaches a plateau of about $2\,\mu\mathrm{m/s}$ for frequencies above 2 Hz. This can be understood as follows. During the repulsive phase, the dumbbell is immotile and the single particle moves as a consequence of the dipole-dipole interaction. Like for the thrower, the force on the particle falls with the distance Y between its centre and that of the dumbbell as $F \sim Y^{-4}$. The distance then increases with time as $Y^5 - Y_0^5 \sim t$ where Y_0 is the distance at the onset of the repulsive phase. The particle reaches a distance Y_1 at the end of the repulsive phase, $Y_1^5 - Y_0^5 = C/f$, where the constant C depends on the strength and fraction of the repulsive interaction, as well as on hydrodynamic drag. The distance by which the particle moves is then $\Delta Y = (C/f + Y_0^5)^{1/5} - Y_0$. During the attractive phase, the dumbbell leaves the wedged position and moves towards the particle. Each of them covers a distance proportional to its mobility ($\Delta x_1/\mu_{11} = -\Delta x_2/\mu_{22}$), where μ_{11} is the mobility of the dumbbell and $\mu_{22} \approx 2\mu_{11}$ that the particle, while the total distance equals $\Delta x_1 - \Delta x_2 = \Delta Y$. Therefore, the dumbbell moves by $\Delta x_1 = \mu_{11}/(\mu_{11}+\mu_{22})\Delta Y$. Note that the expression holds for the wedged rower – in the case of the free rower the backward movement during the repulsive phase needs to be subtracted. Finally, its average velocity is

$$v = f\Delta x_1 = f\frac{\mu_{11}}{\mu_{11}+\mu_{22}}\left(\left(\frac{C}{f}+Y_0^5\right)^{1/5} - Y_0\right) . \quad (6)$$

A good fit of the experimental data (Figure 6) is obtained with the values $C = 4.7 \times 10^5\,\mu\mathrm{m}^5\mathrm{s}^{-1}$ and $Y_0 = 10\,\mu\mathrm{m}$. The fitted Y_0 is larger than the distance between the particle and the dumbbell at the onset of the repulsive phase ($1.5a_2 \approx 4\,\mu\mathrm{m}$). One reason for the discrepancy is the fact that a wedged dumbbell initially exerts a smaller ($\sim 1/2$) force on the particle than a point dipole would. Adhesion between particles can also contribute to the deviation.

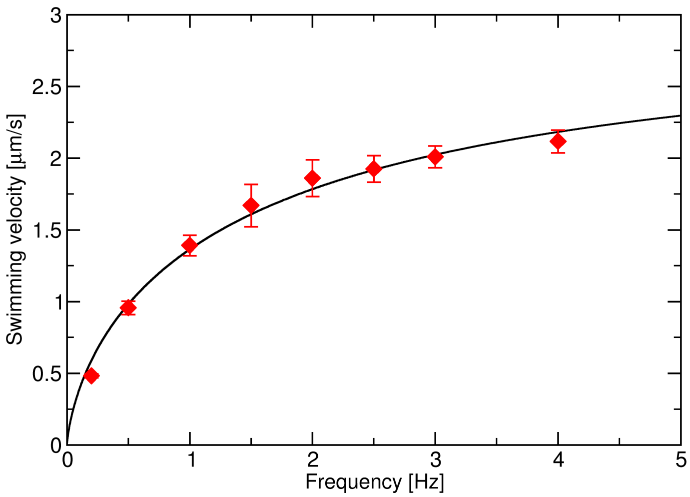

Fig. 6 Measured swimming velocity of the wedged rower as a function of the cycle frequency

The bidirectional rower moves in a direction prescribed by the orientation of the attractive field. It can be made omnidirectional by replacing the static horizontal field with one that rotates fast in the horizontal plane, making the attractive interaction effectively isotropic. However, the rower's orientation is subject to noise and its motion is best described as active Brownian motion[39]. Such a swimmer randomly swims in the plane and to achieve controlled 2D motion and to demonstrate its omnidirectional nature, the swimmer is placed in a circular microfluidic channel (Figure 7). The swimmer finds its way around the loop while being powered by a steady magnetic field sequence[†].

Conclusions

We have created two types of magnetically driven artificial swimmers that swim at low Reynolds number. Both are actuated by field sequences that alternate between an attractive and a repulsive interaction. The first type, the *thrower*, consists of two magnetic beads that differ in size and breaks the time reversal symmetry through a combined effect of gravity and the proximity to a no-slip boundary (glass surface). The second swimmer, the *rower*, breaks the symmetry by reorienting the dumbbell between the attractive and the repulsive phase. We have demonstrated its motion along a circular prefabricated path, which the swimmer follows without requiring any adaptations in the magnetic field sequence. Besides the larger ferromagnetic particles that partially rely on inertia for their rolling[32], we report to the best of our knowledge the first omnidirectional magnetically actuated swimmers. This makes them interesting for studying collective dynamics, and also for applications where a number of agents all driven by the same field can navigate simultaneously through a complex microfluidic network.

Conflicts of interest

There are no conflicts to declare.

Acknowledgements

The authors acknowledge the financial support from the Slovenian Research Agency (ARRS P1-0192, P1-0099 and J1-6724) and COST Action MP1305. We thank Jurij Kotar, Igor Poberaj and Dušan Babić for their contribution to the experimental set-up.

Appendix: Numerical simulation

The simulations were based on overdamped Langevin dynamics. The magnetic moment of a bead was determined as

$$\vec{m}_i = \mu_0 V_i \chi_i \vec{B} \, . \quad (7)$$

The magnetic forces were calculated by taking into account the dipole-dipole interaction between the particles. In addition, each particle was subject to gravity $\vec{F}_i^g = -(\rho_i - \rho_{\mathrm{H_2O}})V_i g \hat{e}_z$. The repulsive force between particles and between a particle and a wall was modelled with a force $F_r = F_0\,[\exp(\Gamma(d_0 - d)) - 1]$ for surface-to-surface distances $d < d_0$, $d_0 = 0.01\,\mu\mathrm{m}$, with $\Gamma = 10^{10}\mathrm{m}^{-1}$ and $F_0 = 10^{-14}\,\mathrm{N}$. The potential was chosen such that its form was insignificant for the result. The parameters used in the simulation are summarised in Table 1.

For bidirectional swimmers, we restricted the motion to the $x-z$ plane. The positions are therefore sufficiently described with a 2-component vector $\vec{x}_i$ and a rotation angle ϕ_i for each particle. The simulated equations of motion were

$$\frac{d}{dt}\begin{pmatrix} \vec{x}_i \\ \phi_i \end{pmatrix} = \begin{pmatrix} \mu_{TT,i} & \mu_{TR,i} \\ \mu_{RT,i} & \mu_{RR,i} \end{pmatrix}\begin{pmatrix} \vec{F}_i \\ \tau_i \end{pmatrix} + k_B T \frac{\partial \mu_{TzTz,i}}{\partial z}\hat{e}_z + \sum_{\alpha=1}^{3}\sqrt{2k_B T \mu_{\alpha,i}^{EV}}\, e_{\alpha,i}\xi_{\alpha,i}(t) \quad (8)$$

with ξ describing uncorrelated white noise $\langle \xi_{\alpha,i}(t)\xi_{\beta,j}(t')\rangle = \delta_{\alpha\beta}\delta_{ij}\delta(t-t')$. The second term compensates the multiplicative nature of the noise term with a position-dependent amplitude. μ_{TT} is the translational mobility tensor in the $x-z$ plane (μ_{TzTz} its z,z component), μ_{RR} the rotational mobility around the y axis and $\mu_{TR,RT}$ the translation-rotation coupling. $\mu_{\alpha,i}^{EV}$ are the eigenvalues of the mobility tensor and $e_{\alpha,i}$ the corresponding eigenvectors. The mobilities were evaluated as described in[36], using the series expansion for $a_i/z_i < 0.98$ and the lubrication approximation from the same reference otherwise. We neglected the hydrodynamic interactions between the particles, which have a minor effect on motility. The equations were solved with a finite difference method with a time step of $\Delta t = 0.25\,\mu\mathrm{s}$.

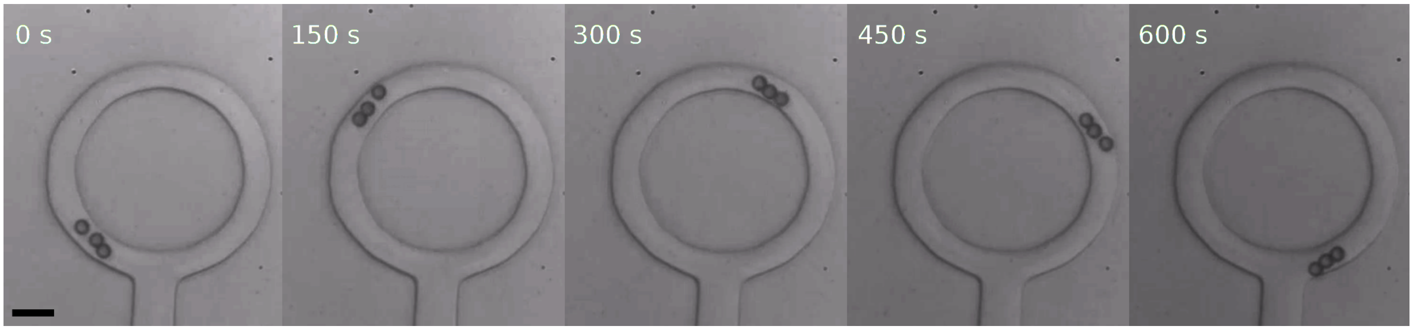

Fig. 7 Time-lapse of the omnidirectional swimmer (rower) in a circular channel. Its motion in the clock-wise direction is driven by a repeating isotropic magnetic field sequence. The cycle frequency is 1.83 Hz and the scale bar is $10\ \mu$m.

Table 1 Parameters used in the simulation

Parameter	Symbol	Value	Notes
Large bead:			
Radius	a_1	$2.25\,\mu$m	[33]
Susceptibility	χ_1	1.63	
Small bead:			
Radius	a_2	$1.35\,\mu$m	
Susceptibility	χ_2	0.756	
Bead density	ρ	$1700\,\mathrm{kg/m^3}$	
Water			
Density	$\rho_{\mathrm{H_2O}}$	$1000\,\mathrm{kg/m^3}$	
Viscosity	η	$0.001\,\mathrm{Pa\,s}$	

References

1 E. M. Purcell, *Am. J. Phys.*, 1977, **45**, 3–11.

2 J. Elgeti, R. G. Winkler and G. Gompper, *Rep. Prog. Phys.*, 2015, **78**, 056601.

3 A. Najafi and R. Golestanian, *Phys. Rev. E*, 2004, **69**, 062901.

4 R. Ledesma-Aguilar, H. Löwen and J. M. Yeomans, *Eur. Phys. J. E*, 2012, **35**, 70.

5 V. A. Vladimirov, *J. Fluid Mech.*, 2013, **716**, 1.

6 B. U. Felderhof, *Eur. Phys. J. E*, 2014, **37**, 096601.

7 J. E. Avron, O. Kenneth and D. H. Oaknin, *New J. Phys.*, 2005, **7**, 234.

8 A. Vilfan and H. Stark, *Phys. Rev. Lett.*, 2009, **103**, 199801.

9 A. D. Gilbert, F. Y. Ogrin, P. G. Petrov and C. P. Winlove, *Quart. J. Mech. Appl. Math.*, 2011, **64**, 239–263.

10 D. Du, E. Hilou and S. L. Biswal, *Soft Matter*, 2018, 862.

11 F. Martínez-Pedrero and P. Tierno, *J. Colloid Interface Sci.*, 2018, **519**, 296–311.

12 K. E. Peyer, L. Zhang and B. J. Nelson, *Nanoscale*, 2013, **5**, 1259–1272.

13 R. Dreyfus, J. Baudry, R. L. Marcus, M. Fermigier, H. A. Stone and J. Bibette, *Nature*, 2005, **437**, 862–865.

14 E. Gauger and H. Stark, *Phys. Rev. E*, 2006, **74**, 382.

15 M. Belovs and A. Cēbers, *Phys. Rev. E*, 2009, **79**, 63.

16 P. Tierno, R. Golestanian, I. Pagonabarraga and F. Sagués, *Phys. Rev. Lett.*, 2008, **101**, 218304.

17 H. Morimoto, T. Ukai, Y. Nagaoka, N. Grobert and T. Maekawa, *Phys. Rev. E*, 2008, **78**, 021403.

18 C. E. Sing, L. Schmid, M. F. Schneider, T. Franke and A. Alexander-Katz, *Proc. Natl. Acad. Sci. U.S.A.*, 2010, **107**, 535–540.

19 F. J. Maier, T. Lachner, A. Vilfan, T. O. Tasci, K. B. Neeves, D. W. M. Marr and T. M. Fischer, *Soft Matter*, 2016, **12**, 9314–9320.

20 A. Ghosh and P. Fischer, *Nano Lett.*, 2009, **9**, 2243–2245.

21 S. Tottori, L. Zhang, F. Qiu, K. K. Krawczyk, A. Franco-Obregón and B. J. Nelson, *Adv. Mater.*, 2012, **24**, 811–816.

22 W. Gao, X. Feng, A. Pei, C. R. Kane, R. Tam, C. Hennessy and J. Wang, *Nano Lett.*, 2013, **14**, 305–310.

23 A. M. Maier, C. Weig, P. Oswald, E. Frey, P. Fischer and T. Liedl, *Nano Lett.*, 2016, **16**, 906–910.

24 U. K. Cheang and M. J. Kim, *Appl. Phys. Lett.*, 2016, **109**, 034101.

25 B. J. Nelson, I. K. Kaliakatsos and J. J. Abbott, *Annu. Rev. Biomed. Eng.*, 2010, **12**, 55–85.

26 J. Li, B. Esteban-Fernández de Ávila, W. Gao, L. Zhang and J. Wang, *Sci. Robot.*, 2017, **2**, eaam6431.

27 W. F. Paxton, K. C. Kistler, C. C. Olmeda, A. Sen, S. K. St. Angelo, Y. Cao, T. E. Mallouk, P. E. Lammert and V. H. Crespi, *J. Am. Chem. Soc.*, 2004, **126**, 13424–13431.

28 S. Nain and N. Sharma, *Front. Life Sci.*, 2015, **8**, 2–17.

29 A. Bricard, J.-B. Caussin, N. Desreumaux, O. Dauchot and D. Bartolo, *Nature*, 2013, **503**, 95–98.

30 B. Dai, J. Wang, Z. Xiong, X. Zhan, W. Dai, C.-C. Li, S.-P. Feng and J. Tang, *Nat. Nano*, 2016, **11**, 1087–1092.

31 D. Ahmed, T. Baasch, B. Jang, S. Pane, J. Dual and B. J. Nelson, *Nano Lett.*, 2016, **16**, 4968–4974.

32 A. Kaiser, A. Snezhko and I. S. Aranson, *Sci. Adv.*, 2017, **3**, e1601469.

33 G. Fonnum, C. Johansson, A. Molteberg, S. Mørup and E. Aksnes, *J. Magn. Magn. Mater.*, 2005, **293**, 41 – 47.

34 J. Kotar, M. Vilfan, N. Osterman, D. Babič, M. Čopič and I. Poberaj, *Phys. Rev. Lett.*, 2006, **96**, 207801.

35 M. Vilfan, A. Potočnik, B. Kavčič, N. Osterman, I. Poberaj, A. Vilfan and D. Babič, *Proc. Natl. Acad. Sci. U.S.A.*, 2010, **107**, 1844–1847.

36 B. Cichocki and R. Jones, *Physica A*, 1998, **258**, 273–302.

37 X. Janssen, A. Schellekens, K. van Ommering, L. van IJzendoorn and M. Prins, *Biosens. Bioelectron.*, 2009, **24**, 1937–1941.
38 J. Happel and H. Brenner, *Low Reynolds Number Hydrodynamics*, Kluwer, 1983.
39 C. Bechinger, R. Di Leonardo, H. Löwen, C. Reichhardt, G. Volpe and G. Volpe, *Rev. Mod. Phys.*, 2016, **88**, 045006.